Proceedings Paper:
Bidar, O., He, P., Anderson, S. orcid.org/0000-0002-7452-5681 et al. (1 more author) (2024) Aerodynamic shape optimisation using a machine learning-augmented turbulence model. In: AIAA SCITECH 2024 Forum. AIAA SCITECH 2024 Forum, 08-12 Jan 2024, Orlando, FL, USA. American Institute of Aeronautics and Astronautics . ISBN 9781624107115

https://doi.org/10.2514/6.2024-1231

Aerodynamic Shape Optimisation Using a Machine Learning-augmented Turbulence Model

Omid Bidar*[1], Ping He†[2], Sean Anderson‡[1], and Ning Qin§[1]

[1]*The University of Sheffield, Western Bank, Sheffield, S10 2TN, UK*
[2]*Iowa State University, Ames, Iowa, 50011, USA*

This paper presents an aerodynamic shape optimisation approach that utilises machine learning techniques to augment the turbulence model for the steady-state Reynolds-averaged Navier-Stokes (RANS) simulations—which are prone to inaccuracies for complex flows involving phenomena such as separation. We employ the field inversion and machine learning (FIML) approach which infers model discrepancies by solving a number of inverse problems (for different shapes and/or flow conditions) given some high-fidelity data, and uses machine learning (such as neural networks) to generalise the discrepancy fields for unseen cases. As a proof-of-concept we use direct numerical simulation (DNS) data for a set of parameterised periodic hills to augment the two-equations $k-\omega$ SST model using FIML, then incorporating it in the CFD solver for aerodynamic shape optimisation where the cost function is the drag minimisation. To illustrate the inherent optimisation sensitivity to the choice of turbulence model, we also use the Wilcox $k-\omega$ model for comparison. Once the optimal shapes are achieved for the different turbulence models, we propose using the hybrid RANS-LES improved delayed detached eddy simulations (IDDES) to validate the flow predictions, which in turn is validated against the available DNS data. Results highlight the sensitivity of optimisation to the turbulence model in the presence of flow separation, and the FIML-augmented $k-\omega$ SST model is able to achieve much higher drag reduction ($20.8-25.3\%$) **with fair agreement to the IDDES predictions (in terms of velocity and skin friction). The baseline SST model achieves a drag reduction of** $4.5-6.5\%$**, and the velocity and skin friction compares poorly to the IDDES results.**

I. Introduction

Aerodynamic shape optimisation based on computational fluid dynamics (CFD) analyses is a vibrant research field and is expected to play a significant role in industry [1, 2], for applications such as modern aerospace vehicles design, more efficient renewable energy solutions (e.g. wind turbines), etc. Turbulence is a ubiquitous flow phenomenon in these applications, which can be numerically simulated using techniques with various levels of fidelity. Low fidelity approaches such as potential-flow or Euler equations ignore viscous effects, while turbulence can be partially or fully resolved in large eddy simulations (LES) and direct numerical simulations (DNS), respectively. As aerodynamic shape optimisation is an iterative process, that requires many function evaluations, LES and DNS are computationally prohibitive. Alternatively, simulations based on the Reynolds-averaged Navier-Stokes (RANS) equations are considered adequate for CFD-based on-design aerodynamic shape optimisation due to their *relative* simplicity, low computational cost, and robustness. However, RANS simulations have well-documented deficiencies for complex flows (e.g. [3]), such as those involving separation, which means the models are inadequate in these scenarios, especially for off-design conditions. In this work, we explore aerodynamic shape optimisation in the presence of a massive flow separation, simulated by a machine learning-augmented RANS-based turbulence model.

Like many areas of science the use of machine learning techniques in aerodynamic shape optimisation has received noticeable attention. Main application areas as identified by Li *et al.* in the recent review are [4]: geometric parameterisation of the design space to exclude aerodynamic shapes which are deemed abnormal, thus allowing the use of fewer design variables; predictions of aerodynamic coefficients leveraging machine-learning-based predictive simulations; and new optimisation architectures, such as replacing CFD-based optimisation with surrogate-based

*PhD candidate, Dept. of Automatic Control and Systems Engineering, and Dept. of Mechanical Engineering, obidar1@sheffield.ac.uk
†Assistant Professor, Department of Aerospace Engineering, AIAA Senior Member
‡Senior Lecturer, Department of Automatic Control and Systems Engineering
§Professor, Department of Mechanical Engineering, AIAA Associate Fellow, n.qin@sheffield.ac.uk

optimisation. However, the use of machine learning techniques in aerodynamic shape optimisation for more accurate turbulence flow predictions in the RANS setting is less well-explored.

Investigation of aerodynamic shape optimisation sensitivity to the choice of turbulence model has shown that while it is less sensitive in on-design conditions with relatively simple flows (e.g. small or no separation, no shock boundary layer interactions, etc.), it can be sensitive in off-design conditions in deterministic optimisation setups (i.e. when uncertainty due to turbulence modelling is unaccounted) [5]. Cook *et al.* investigated performing shape optimisation while accounting for structural uncertainties in turbulence closure modelling through the eigenspace perturbation approach [6]. They concluded that performing design optimisation under turbulence model uncertainty can lead to more robust solutions, and avoids sub-optimal designs where turbulence model sensitivities are unaccounted.

Shortfalls of existing turbulence models in RANS-based simulations can be categorised as parametric (arising from the turbulence model constants tuned on a limited set of canonical flows); functional (due to the PDE form of the turbulence model variables such as turbulent kinetic energy k etc.); and structural (due to simplifying modelling assumptions, such as the Boussinesq hypothesis employed in eddy-viscosity models) [7]. In recent years there has been a surge in the application of data-driven and machine learning techniques to address the errors in all three categories. For instance, novel machine learning architectures with embedded invariance properties for eddy viscosity Reynolds stress models based on isotropic basis tensors [8, 9]; and formulation of algebraic nonlinear closures using gene expression programming and symbolic regression [10–12]. These have been extensively reviewed in the following papers: [7, 13, 14].

One approach to turbulence model augmentation is field inversion and machine learning (FIML) [15–18], which we use in this work. In this approach the transport equation(s) for an existing turbulence model is modified by a corrective factor. Then, given some high-fidelity data, field inversion is performed for a number of flows with varying flow conditions (e.g. Reynolds number, angle of attack for a wing/airfoil, etc.) and/or geometries. In essence, field inversion is a variational (also called adjoint-based) data assimilation approach, and has been successfully applied by many researchers for turbulent mean flow reconstruction [19–22]. Ensemble-based field inversion has also been concurrently pursued by other researchers, for example [23–25]. Field inversion-based flow reconstruction is case specific, i.e. it cannot be used for prediction of unseen flows. Therefore, machine learning approaches such as deep neural networks (e.g. [17]) or Gaussian processes (e.g. [16]) are used to generalise the model corrections for unseen flow conditions/geometries for predictions. Benefits of the FIML approach are model-consistency, and the ability to work with relatively sparse data, e.g. [17, 22].

Inspired by the FIML approach, Fidkowski recently investigated aerodynamic shape optimisation for unsteady turbulent flows [26]. The *unsteady* RANS-based turbulent flow simulations (with the existing Spalart-Allmaras model) are used as training data to correct the steady RANS-based flow simulations. The design objective and constraints were time-averaged quantities. The results achieved demonstrated that accounting for unsteady flow behaviour leads to improved designs, compared to steady flow simulations. However, it is important to note that the unsteady reference data used in this methodology was still based on the eddy viscosity-based turbulence closure which means that the aforementioned parametric, functional and structural shortfalls in the model still exists. In this work we augment an existing steady turbulence model ($k-\omega$ SST) trained on time-averaged high-fidelity simulation data from DNS thus addressing the short-falls inherent in the RANS-based predictions. Admittedly, generating the DNS results is computationally very expensive, however, we are currently investigating the use of hybrid RANS-LES [27] (which are considerably cheaper than DNS or wall-resolved LES) simulations for generating the high-fidelity training data.

The rest of the paper is structured as follows. Starting with an overview of the proposed methodology, in Section II we describe the RANS-based turbulence model, the field inversion and machine learning approach, the aerodynamic shape optimisation setup, and the hybrid RANS-LES model for validating the optimal shape flow predictions. Results are presented and discussed in Section III and finally conclusions are drawn and future works outlined in Section IV.

II. Methods

A. Overview

An overview of the proposed methodology for aerodynamic shape optimisation is outlined in Fig. 1. We start by introducing the periodic hill test case in Section II.B, followed by the governing equations and the baseline turbulence model, $k-\omega$ SST in Section II.C. Then, the baseline model augmentation is introduced through field inversion and machine learning in Section II.D. The aerodynamic shape optimisation problem is formulated in Section II.E, and shape optimisation is performed using the baseline SST model, the FIML-augmented SST model, and the Wilcox $k-\omega$ model.

Finally, the framework for validating the flow predictions with a higher fidelity simulation (improved delayed detached eddy simulation, IDDES) is outlined in Section II.F.

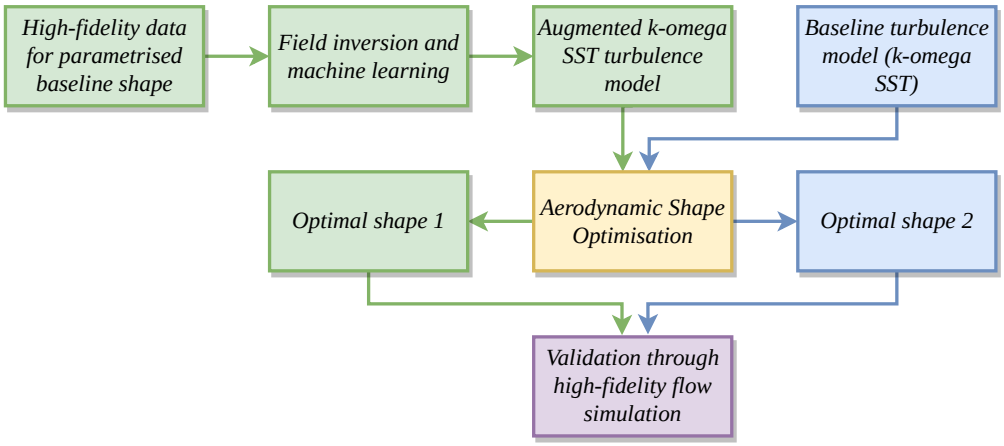

Fig. 1 Overview of the proposed methodology for aerodynamic shape optimisation using machine learning-augmented turbulence model.

B. Proof-of-concept test case: periodic hill

To test the proposed framework, we select the periodic hill case. This choice is driven by the public availability of high-fidelity data (DNS) for a set of parameterised geometries involving complex flow features that are not accurately predicted by most existing eddy-viscosity models.

Fig. 2 illustrates the five parameterised configurations (with modification parameter, α) by Xiao *et al.* [28]. The configurations involved mild to massive flow separation due to the presence of the hills. The baseline geometry ($\alpha = 0.1$) has been widely studied, experimentally ([29]), and using high-fidelity simulations (e.g. DNS ([30], LES [31]) for a range of Reynolds numbers, and has become a prototypical test case for investigating data-driven turbulence models. The hill steepness is systematically varied by stretching/contracting the hill width in the streamwise direction as a function of α, where the total horizontal length L_x, normalised by the constant hill crest height, H, is given by:

$$L_x/H = 3.858\alpha + 5.142. \tag{1}$$

In the RANS simulations, the flow is assumed two dimensional, with no-slip boundary conditions at the upper and

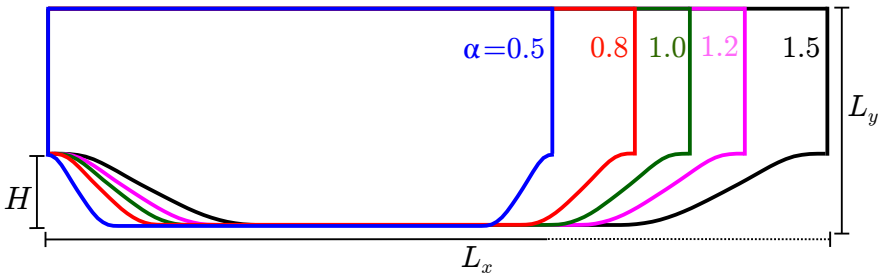

Fig. 2 Parameterised periodic hill geometries.

lower walls, and cyclic boundary conditions at the hills. Structured meshes, with 14,751 cells, provided by Xiao *et al.* [28] are used. A constant bulk velocity is maintained in the streamwise direction by adding a forcing term in the x-momentum equation, where the bulk Reynolds number is defined as:

$$Re_b = \frac{U_b H}{\nu}, \qquad U_b = \frac{1}{2.035H}\int_H^{3.035H} U_x\,(y)\,dy, \tag{2}$$

where U_b is the bulk velocity, ν is the kinematic viscosity, and U_x is the streamwise velocity component.

Table 1 outlines the geometries used for training in the preliminary results reported at present. In the final paper, we will investigate how the results are affected if fewer geometries are used in the training.

Table 1 Geometries used for training and testing FIML implementation.

Training cases	Testing case
$\alpha = \{0.5, 0.8, 1.2, 1.5\}$	$\alpha = 1.0$

C. RANS equations and the $k-\omega$ SST model

The steady, incompressible Reynolds-averaged Navier-Stokes equations are expressed as follows, and solved using the SIMPLE algorithm in OpenFOAM:

$$\nabla \cdot \boldsymbol{U} = 0, \tag{3}$$

$$\nabla \cdot (\boldsymbol{U}\boldsymbol{U}) + \nabla p - \nu_{\text{eff}} \nabla \cdot \left(\nabla \boldsymbol{U} + \nabla \boldsymbol{U}^T \right) = 0, \tag{4}$$

where $\boldsymbol{U}$ is the velocity, p is the pressure, $\nu_{\text{eff}} = \nu + \nu_t$ is the effective viscosity with ν and ν_t representing the molecular and turbulent kinematic viscosity, respectively.

The RANS closure used is the popular two-equation linear eddy-viscosity $k-\omega$ SST model. The SST model is a synergy of the standard $k-\epsilon$ and the Wilcox $k-\omega$ models, blending the freestream independence of the former, and the improved predictions in the near-wall boundary layer of the latter. The turbulent kinematic viscosity ν_t in Eqn. 4 is calculated as follows:

$$\nu_t = a_1 \frac{k}{\max\left(a_1 \omega, S F_2\right)}, \tag{5}$$

where k is the turbulent kinetic energy, ω is the turbulence dissipation rate, S is the strain rate, F_2 is a blending function, and $a_1 = 0.31$ is a constant.

The transport equations for the turbulent kinetic energy k and turbulent dissipation ω are:

$$\frac{\partial k}{\partial t} + \frac{\partial k}{\partial x_j} = P_k - \beta^* k\omega + \frac{\partial}{\partial x_j}\left[(\nu + \sigma_k \nu_t) \frac{\partial k}{\partial x_j} \right], \tag{6}$$

$$\frac{\partial \omega}{\partial t} + \frac{\partial \omega u_j}{\partial x_j} = \frac{\gamma}{\nu_t} P_k - \beta \omega^2 + \frac{\partial}{\partial x_j}\left[(\nu + \sigma_\omega \nu_t) \frac{\partial \omega}{\partial x_j} \right] + 2(1 - F_1)\sigma_{\omega 2} \frac{1}{\omega} \frac{\partial k}{\partial x_i} \frac{\partial \omega}{\partial x_i}, \tag{7}$$

$$P_k = \mu_t \left(\frac{\partial u_i}{\partial x_j} + \frac{\partial u_j}{\partial x_i} \right) \frac{\partial u_j}{\partial x_i} - \frac{2}{3} \rho k \frac{\partial u_j}{\partial x_i}, \tag{8}$$

where P_k represents the production of turbulent kinetic energy, F_1 is another blending function, ρ is the density, μ_t is the dynamic turbulent viscosity, β^*, σ_k, γ, β, σ_ω, and $\sigma_{\omega 2}$ are constants—refer to [32, 33] for details.

D. Field inversion and machine learning

The field inversion and machine learning framework [16–18] for turbulence model augmentation involves the following steps: solving a number of inverse problems to reconstruct turbulent mean flows given some high-fidelity data for a quantity/quantities of interest; generalise the reconstruction using deep learning for cases beyond the training dataset; and finally embedding the augmented model in a RANS solver for improved predictions, as outlined in Fig. 3.

1. Field inversion

In field inversion the turbulent flow reconstruction is performed by perturbing one of the transport equations in the turbulence model, in this instance ω, by a scalar field β_{FI}. The transport equation for the turbulence dissipation is thus expressed as follows in the general form:

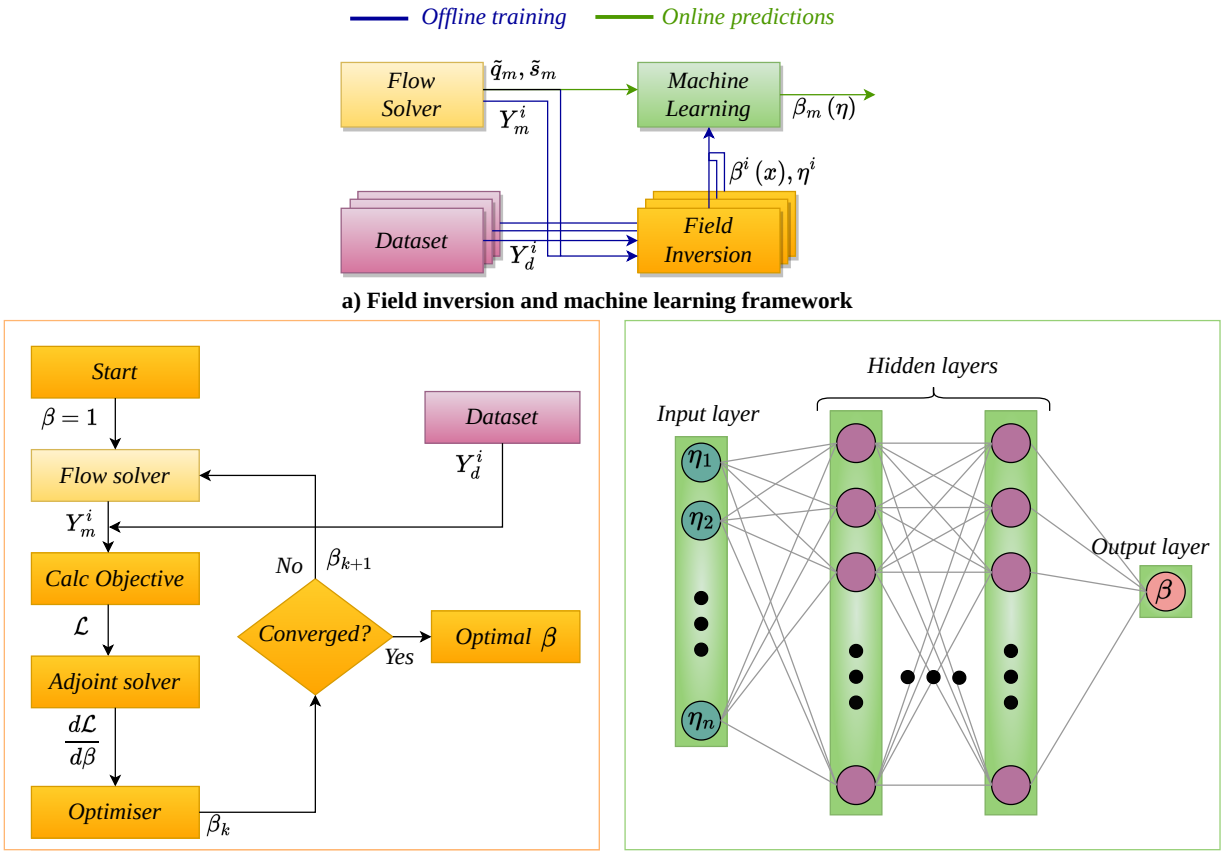

Fig. 3 Graphical overview of the field inversion and machine learning framework.

$$\frac{D\omega}{Dt} = \beta_{\mathrm{FI}}(\boldsymbol{x})\,\mathcal{P}(\omega, \boldsymbol{w}) + \mathcal{T}(\omega, \boldsymbol{w}) - \mathcal{D}(\omega, \boldsymbol{w}), \tag{9}$$

where $\mathcal{P}$, $\mathcal{T}$, and $\mathcal{D}$ are the production, transport, and dissipation terms of the transport equation respectively, as shown in Eqn. 7.

Optimum values for β_{FI} is sought in all the mesh cells by minimising an objective function of the following form:

$$\min_{\beta_{\mathrm{FI}}} \quad \mathcal{L} = \|\mathcal{G}(\beta_{\mathrm{FI}}) - \boldsymbol{d}\|_2^2 + \lambda\|\beta_{\mathrm{FI}} - 1.0\|_2^2, \tag{10}$$

where $\|\cdot\|_2$ is the $L2$ norm, λ is a relaxation or regularisation parameter to bias the solution closer to the baseline model and to avoid an ill-posed optimisation problem. In the present results, the data used for training are the streamwise velocity fields for the hill geometries given in Table 1. In terms of software implementation, we employ our open-source tool, previously introduced in [34].

2. Machine learning formulation

The discrepancy field $\beta_{\mathrm{FI}}(\boldsymbol{x})$ inferred in the field inversion step is only applicable to the flow conditions and the particular geometry it has been applied to, and cannot be extended for predictions for a different case. In order to allow for the predictive capability, the corrective fields must be generalised in terms of non-dimensional flow features. This has previously been achieved using machine learning techniques, where an additional optimisation problem is solved, through back-propagation, for instance:

$$\min_{\boldsymbol{w}} \quad \mathcal{L}[\beta_{\mathrm{FI}}^i(\boldsymbol{x}), \beta_{\mathrm{ML}}(\eta, \boldsymbol{w})], \tag{11}$$

with $\boldsymbol{w}$ representing the trainable parameters, e.g. weights and biases in a deep neural network, and where the goal to is to map the corrective fields β_{FI} from the spatial coordinates to non-dimensional features space η. The flow features used in this work are shown in Table 2, some or all of which have been used in many previous works [28, 35–37], and found to be useful.

Table 2 Features used as neural network inputs.

Feature	Description	Formula	Normalisation
η_1	Q-criterion	$\frac{1}{2}\left(\|\boldsymbol{\Omega}\|^2 - \|\boldsymbol{S}\|^2\right)$	$\|\boldsymbol{S}\|^2$
η_2	Turbulence intensity	k	$\frac{1}{2}U_iU_i$
η_3	Wall-distance based Reynolds number	$\min\left(\frac{\sqrt{k}d}{50\nu}, 2\right)$	not applicable
η_4	Pressure gradient along streamline	$U_k\frac{\partial P}{\partial x_k}$	$\sqrt{\frac{\partial P}{\partial x_j}\frac{\partial P}{\partial x_j}U_iU_i}$
η_5	Ratio of pressure normal stresses to shear stress	$\sqrt{\frac{\partial P}{\partial x_i}\frac{\partial P}{\partial x_i}}$	$\frac{1}{2}\rho\frac{\partial U_k^2}{\partial x_k}$
η_6	Non-orthogonality between velocity and its gradient	$\lvert U_iU_j\frac{\partial U_i}{\partial x_j}\rvert$	$\sqrt{U_lU_lU_i\frac{\partial U_i}{\partial x_j}U_k\frac{\partial U_k}{\partial x_j}}$
η_7	Ratio of total to normal Reynolds stress	$\|\overline{u_i'u_j'}\|$	k
η_8	Streamline curvature	$\lvert\frac{D\boldsymbol{\Gamma}}{Ds}\rvert$ where $\boldsymbol{\Gamma}\equiv\boldsymbol{U}/\lvert\boldsymbol{U}\rvert$, $Ds=\lvert\boldsymbol{U}\rvert Dt$	$\frac{1}{L_c}$
η_9	Ratio of convection to production of TKE	$U_i\frac{dU}{dx_i}$	$\lvert\overline{u_j'u_k'}S_{jk}\rvert$

While a number of machine learning techniques are applicable, in this work we use a fully-connected deep neural network. The neural network results shown here used 10 hidden layers, 100 nodes per layer, with the hyperbolic tangent activation function, and the R^2 loss function. TensorFlow was used for the neural network implementation, and coupled with OpenFOAM using a similar approach to Maulik *et al.* [38].

E. Aerodynamic shape optimisation

We solve an aerodynamic shape optimisation problem where the goal is to optimise the lower wall for minimum drag. This objective function formulation for this particular case is more of a mathematical construct than an application of aerodynamic engineering design optimisation. We stress that the goal is to assess the proposed framework in the presence of complex flow structures which are encountered in engineering applications, making this proof-of-concept case a suitable one, nonetheless.

The objective functions and constraints are defined as follows:

$$\begin{aligned}
&\min_{\Delta y} \quad C_{d,\text{lower wall}} = \frac{1}{\frac{1}{2}\rho U_b^2 S}\left(\iint_S \tau_w(\hat{t}\cdot\hat{i})\mathrm{d}s + \iint_S p(\hat{n}\cdot\hat{j})\mathrm{d}s\right), \\
&\text{subject to} \quad -0.4 \le \Delta y/H \le 0.4, \quad \nabla p = \nabla p_{\text{prescribed}}, \quad T.B. = \sum_{i=1}^{N_{cells}} \phi V_i \nu_{t,i} \ge T.B._{\text{prescribed}}, \quad \phi = 10^3,
\end{aligned} \tag{12}$$

where Δy (representing the manipulation of the lower wall in the y-direction) is the design variable, and C_d is the drag coefficient. The unit vectors $\hat{i}$, $\hat{j}$, $\hat{t}$ and $\hat{n}$ represent the directions parallel and perpendicular to the bulk velocity, U_b. τ_w, p, ρ, and S are the wall shear stress, wall pressure, density, and surface area. The constraints are the upper and lower bounds for the possible y-coordinates values, the prescribed pressure gradient to achieve a constant bulk flow (as described in Eqn. 2), and the sum of turbulent viscosity over the entire flow field. The last constraint, $T.B.$, is used to penalise the optimiser tendency to essentially turn the lower wall into flat wall to reduce the drag by eliminating the flow separation. This is to ensure that a certain turbulence level continues to characterise the flow.

In terms of the aerodynamic shape optimisation implementation we utilise DAFoam [39] (also used in field inversion), which couples many open-source modules required for gradient-based multi-disciplinary design optimisation utilising the discrete adjoint approach for efficient gradient calculations—refer to [39] for detailed workflow description in DAFoam. Finally, the geometry is parameterised using the free-form deformation (FFD) approach, shown in Fig. 4.

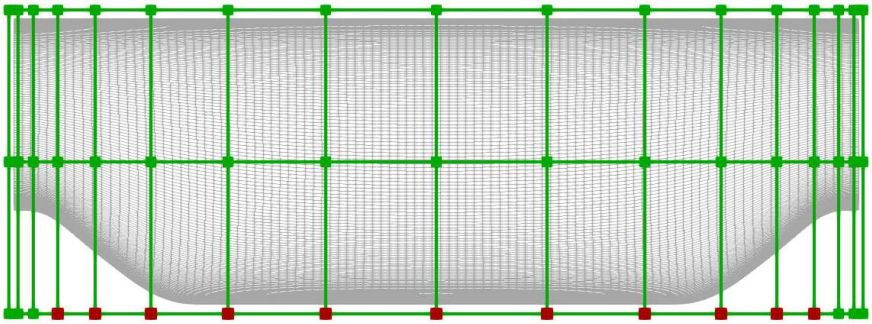

Fig. 4 The structured mesh for the periodic hill case, overlayed by the FFD points. Red squares represent the FFD control points that are allowed to move to morph the surface.

F. Surrogate truth model: Spalart-Allmaras IDDES

Once the aerodynamic shape optimisation is performed, it is important to validate the predictive capabilities of the different turbulence models using a higher-fidelity method. In this work, we use a hybrid RANS/LES approach as the truth model. Hybrid methods utilise a closure model in the near-wall region of the flow, while performing eddy-resolving simulation away from the wall. The predictions with these methods can be significantly more accurate than RANS models, while requiring a coarser mesh than required for wall-resolved LES, or DNS [27, 40].

The particular hybrid approach we use is the Spalart-Allmaras improved delayed detached eddy simulation (IDDES). The PDE for the Spalart-Allmaras IDDES, defined as a function of the surrogate eddy viscosity $\tilde{\nu}$ is given as [41]:

$$\frac{\partial \tilde{\nu}}{\partial t} + U_i \frac{\partial \tilde{\nu}}{\partial x_j} = c_{b1}\tilde{S}\tilde{\nu} + \frac{1}{\sigma}\left[\nabla \cdot (\tilde{\nu}\nabla\tilde{\nu}) + c_{b2}\,(\nabla\tilde{\nu})^2\right] - c_{w1} f_w \left(\tilde{r}\left(\frac{\tilde{\nu}}{l_{\text{IDDES}}}\right)^2\right), \tag{13}$$

where the turbulent eddy viscosity is defined as $\nu_t = f_{v1}\tilde{\nu}$. The functions f_{v1} and f_w are for near-wall corrections, $\tilde{S}$ is the strain rate tensor, the non-dimensional term $\tilde{r}$ is defined as $\nu_t/(\tilde{S}\kappa^2 d_w^2)$, where κ is the von Kármán constant, d_w is the distance from the wall, and $\{\sigma, c_{b1}, c_{b2}, c_{w1}\}$ are model constants. The modified length scale l_{IDDES} is used to switch the transition from the unsteady RANS to scale-resolving LES, and along with the intermediate variables and functions, is defined as:

$$l_{\text{IDDES}} = \tilde{f}_d\,(1 + f_e)\,d_w + (1 - \tilde{f}_d) l_{\text{LES}}, \tag{14a}$$

$$l_{\text{LES}} = C_{\text{DES}}\psi\Delta, \quad C_{\text{DES}} = 0.65, \tag{14b}$$

$$\Delta = \min(\max([C_w d_w, C_w h_{\max}, h_{wn}])), \tag{14c}$$

$$\tilde{f}_d = \max(1 - f_d, f_B), \tag{14d}$$

$$f_d = 1 - \tanh\left[8\left(r_d^3\right)\right], \tag{14e}$$

$$f_B = \min\left[2\exp\left(-9\alpha^2\right), 1.0\right], \tag{14f}$$

$$\alpha = 0.25 - \frac{d_w}{h_{\max}}, \tag{14g}$$

$$f_e = \max\left[(f_{e1} - 1), 0\right]\psi f_{e2}, \tag{14h}$$

for detailed discussions refer to Shur *et al.* [41].

For the preliminary results in this abstract, we only consider the S-A model, however, we will also investigate the $k - \omega$ SST IDDES for the final paper. Additionally, to ensure the training and validation turth models are consistent, in the final paper we will replace the DNS data with the IDDES results, while still validating the IDDES results against the DNS.

The three-dimensional mesh employed is extruded by $L_x/2$ in the spanwise direction, with periodic boundary conditions. The total number of mesh cells are: $N_x \times N_y \times N_z = 400 \times 220 \times 80 = 7.04 \times 10^6$.

III. Results and Discussions

A. Baseline shape

First, we present results for the baseline periodic hill geometry, $\alpha = 1.0$ in Fig. 2. We compare quantities of interest predicted by the three RANS-based turbulence models ($k-\omega$ SST, FIML-augmented $k-\omega$ SST and Wilcox $k-\omega$), and the hybrid RANS-LES (IDDES) using the Spalart-Allmaras model which will be used for validation of flow predictions of the optimised shapes. We quantify the error in these predictions against DNS results from Xiao *et al.* [28] (dataset used for training the FIML-augmented $k-\omega$ SST model, as described in Section II.B), and the DNS wall quantity data (surface pressure and skin friction) from Krank *et al.* [42], since these are not available from [28]. The skin friction and surface pressure, C_f and C_p, respectively, are defined as,

$$C_f = \frac{\rho\nu \boldsymbol{t}^T \cdot (\nabla \boldsymbol{U} \cdot \boldsymbol{n})}{\frac{1}{2}\rho U_b^2}, \qquad C_p = \frac{p - p_0}{\frac{1}{2}\rho U_b^2}, \tag{15}$$

where ρ is the fluid density, $\boldsymbol{U}$ is the velocity, $\boldsymbol{t} = [t_1, t_2, t_3]^T$ and $\boldsymbol{n} = [n_1, n_2, n_3]^T$ are the tangential and wall-normal vectors, and p_0 is the pressure at the hill crest $(x/H, y/H) = (0, 1)$.

Table 3 Comparison of root-mean-square error between different models and reference DNS data for the *baseline shape*. The velocity and Reynolds stress DNS data are from Xiao *et al.* [28], while the surface data are from Krank *et al.* [42].

Quantity	RMSE $k-\omega$ SST	RMSE FIML $k-\omega$ SST	RMSE Wilcox $k-\omega$	RMSE S-A IDDES
Streamwise velocity	0.92381	0.32672	0.57346	0.30831
Wall-normal velocity	0.18535	0.08797	0.06988	0.03910
Reynolds stress (normal)	0.33238	0.14572	0.12966	0.04056
Reynolds stress (shear)	1.82788	0.03320	0.03248	0.00858
Surface friction, hill wall	0.00339	0.00205	0.00476	0.00103
Surface pressure, hill wall	0.16991	0.07869	0.04342	0.11662

Table 4 Comparison of drag coefficient predictions using the different RANS models for the *baseline shape*. The final column shows the percentage error in the total drag with respect to the IDDES predictions.

Turbulence model	Pressure drag, $C_{d,p}$	Viscous drag, $C_{d,v}$	Total drag, C_d	Error
IDDES Spalart-Allmaras	0.033883	0.000982	0.034866	-
$k-\omega$ SST	0.037437	0.000408	0.037844	8.54%
FIML-augmented SST	0.038481	0.000907	0.039387	12.97%
Wilxoc $k-\omega$	0.050553	0.001528	0.052081	49.37%

The root-mean-square error results in Table 3, and the drag predictions in Table 4 are summarised as follows:

1) Of the two baseline turbulence models considered–$k-\omega$ SST and Wilcox $k-\omega$–the later is more accurate for all the quantities considered, except the surface friction.
2) The FIML-augmented $k-\omega$ SST model significantly reduces the errors in all the quantities compared to the baseline SST.
3) IDDES results have significantly lower errors compared to the reference DNS data for all quantities, except the surface pressure. It is unclear at present what causes this significant difference. The Wilcox $k-\omega$ model is the closest to the DNS data from Krank *et al.* [42]. This discrepancy will also be reflected in the surface drag predictions in Table 4.
4) The dominant component in the total drag are from the pressure forces. The aforementioned discrepancy in surface pressure predictions from IDDES will skew the drag coefficient errors reported in Table 4.

5) All the RANS-based turbulence models over-predict the drag coefficient, especially the Wilcox $k-\omega$, which is consistent with the surface pressure distribution shown in Fig. 5.
6) The baseline $k-\omega$ SST drag prediction is the closest to the IDDES result, despite the discrepancies in all other quantities reported in Table 3. This can be misleading, since the surface pressure and friction predictions by the baseline SST model is very poorly predicted compared to the other RANS-based models, and the reference DNS data, as shown in Fig. 5.
7) The viscous drag component from FIML-augmented $k-\omega$ SST is closest to the respective component from IDDES. This can be explained by the consistently close match in the velocity predictions as shown in Fig. 6, and Table 3. This is anticipated given that the viscous forces are a function of the velocity (see the expression for C_f in Eqn. 15) and the FIML model is trained on the streamwise velocity field data from DNS.

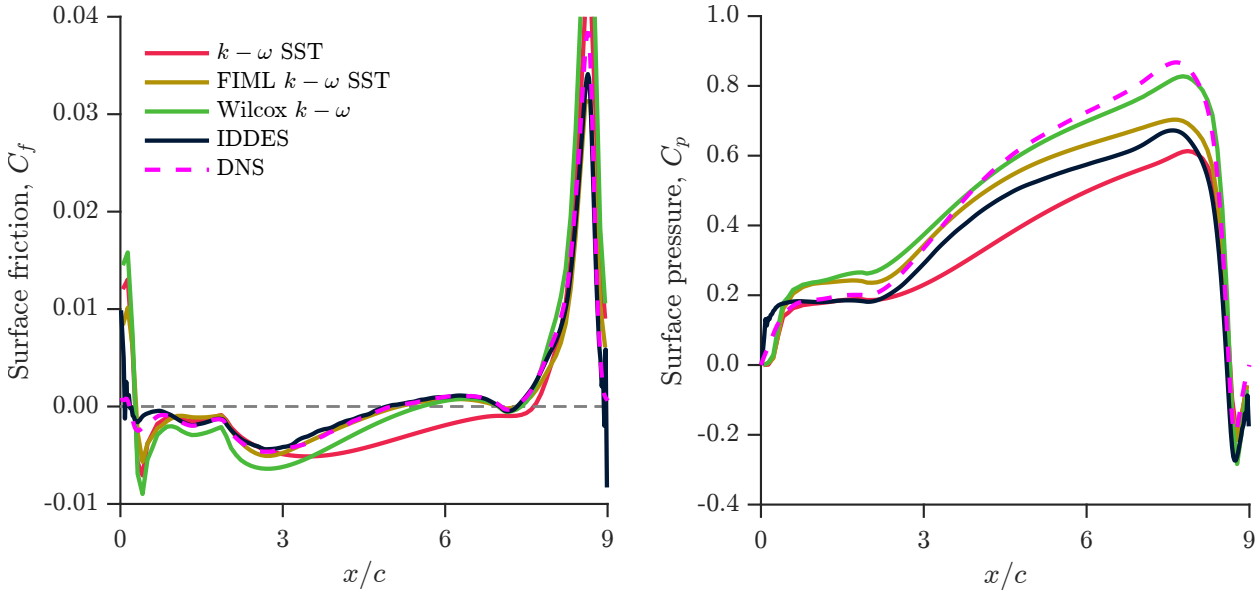

Fig. 5 Comparison of the surface quantities on the hill wall for the baseline periodic shape. The DNS data are from Krank *et al.* [42].

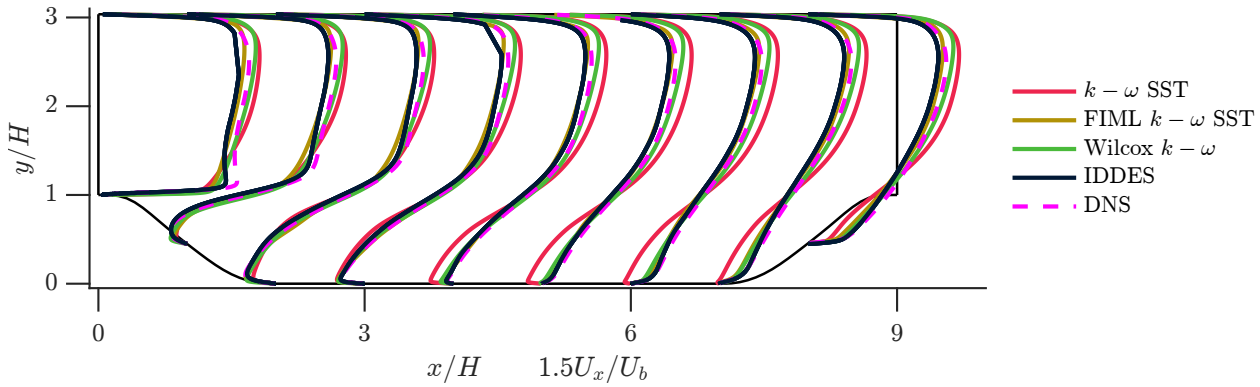

Fig. 6 Comparison of the streamwise velocity profiles for the baseline periodic shape. The DNS data are from Xiao *et al.* [28].

The surface pressure and surface drag predictions on the lower wall (hills) are shown in Fig. 5. Both the baseline RANS-based turbulence models are unable to accurately predict the surface friction. While the Wilcox $k-\omega$ model predicts the reattachment somewhat accurately, it fails to capture the skin friction in the region of separated flow near the initial hill. The baseline $k-\omega$ SST skin friction prediction are most erroneous, as it significantly over-predicts the

flow separation in the shear layer, resulting in a much delayed flow reattachment location. The FIML-augmented $k-\omega$ SST model is able to match the DNS data on the flat portion of the lower wall, while some discrepancies are present on the hills. The IDDES results also match the DNS reference very well. In terms of surface pressure predictions, the baseline $k-\omega$ SST is once again very inaccurate in the separated region (particularly on the flat surface between the hills). The Wilcox $k-\omega$ on the other hand is close to the reference DNS, followed by the FIML-augmented $k-\omega$ SST. Unfortunately, as stated previously, the IDDES pressure predictions do not compare well with the reference DNS. The causes for this require further investigation.

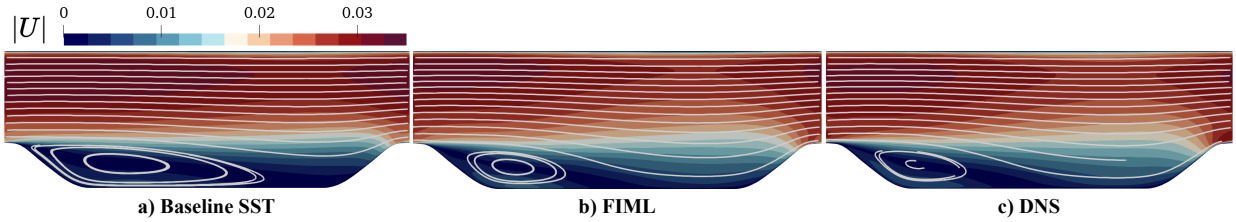

Fig. 7 Velocity fields comparison for the baseline periodic hill case ($\alpha = 1.0$).

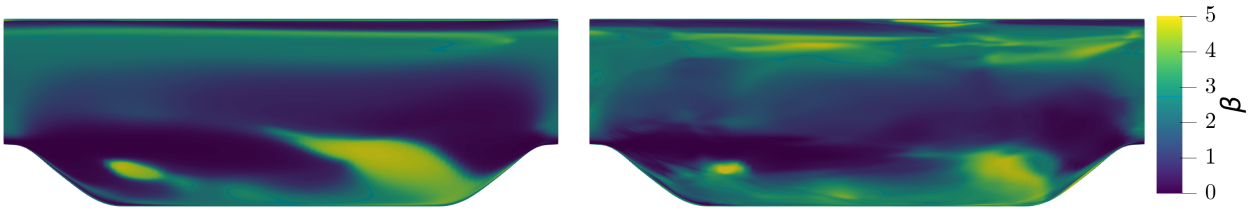

Fig. 8 Corrective field β comparison between field inversion (left) and FIML model prediction (right) for the PH test case ($\alpha = 1.0$).

Fig. 6 shows the streamwise velocity profiles. The baseline $k-\omega$ SST is clearly the least accurate. It consistently struggles to accurately capture the flow in the separated shear layer, and over-predicts the size of the separation bubble, as further illustrated by the streamlines in Fig. 7. The Wilcox $k-\omega$ is more accurate compared to the baseline SST in the separated flow region near the lower wall. The FIML-augmented $k-\omega$ SST is able to match the DNS data fairly well. The IDDES results match the DNS very well.

Finally, for reference we show the corrective field, β, in the FIML-augmented SST model in Fig. 8. As mentioned previously, when training the FIML model, we do not use the data for the baseline periodic hill shape ($\alpha = 1.0$). For reference we show the β field from field inversion in Fig. 8. While there are discrepancies between the field inversion and the neural network-predicted corrective fields, we did not observe major differences in the predictions of physical quantities of interest (e.g. velocity, surface quantities such as the skin friction, and turbulence variables), as the augmented SST model is not too sensitive to these differences.

B. Optimised shapes

The aerodynamic shape optimisation results using the three turbulence models considered, $k-\omega$ SST, FIML-augmented $k-\omega$ SST, and the Wilcox $k-\omega$ model will be presented in this section, with comparisons to IDDES predictions.

The optimised shapes, along with lower wall pressure and skin friction distributions are shown in Fig. 9. Tables 5 and 6 show comparisons of the drag coefficients. Contours of streamwise velocity, and the streamlines for the RANS models and IDDES results are shown in Fig. 10, with velocity profiles comparisons in Fig. 11. Finally, turbulent flow structures are illustrated through Q-criterion contours from IDDES in Fig. 12. The key findings are summarised as follows:

1) The choice of turbulence model for flow predictions clearly impacts the aerodynamic shape optimisation outcome, as the three models result in three distinct “optimal" shapes. The FIML-augmented $k-\omega$ and the Wilcox $k-\omega$ share some similarities which we will discuss shortly.

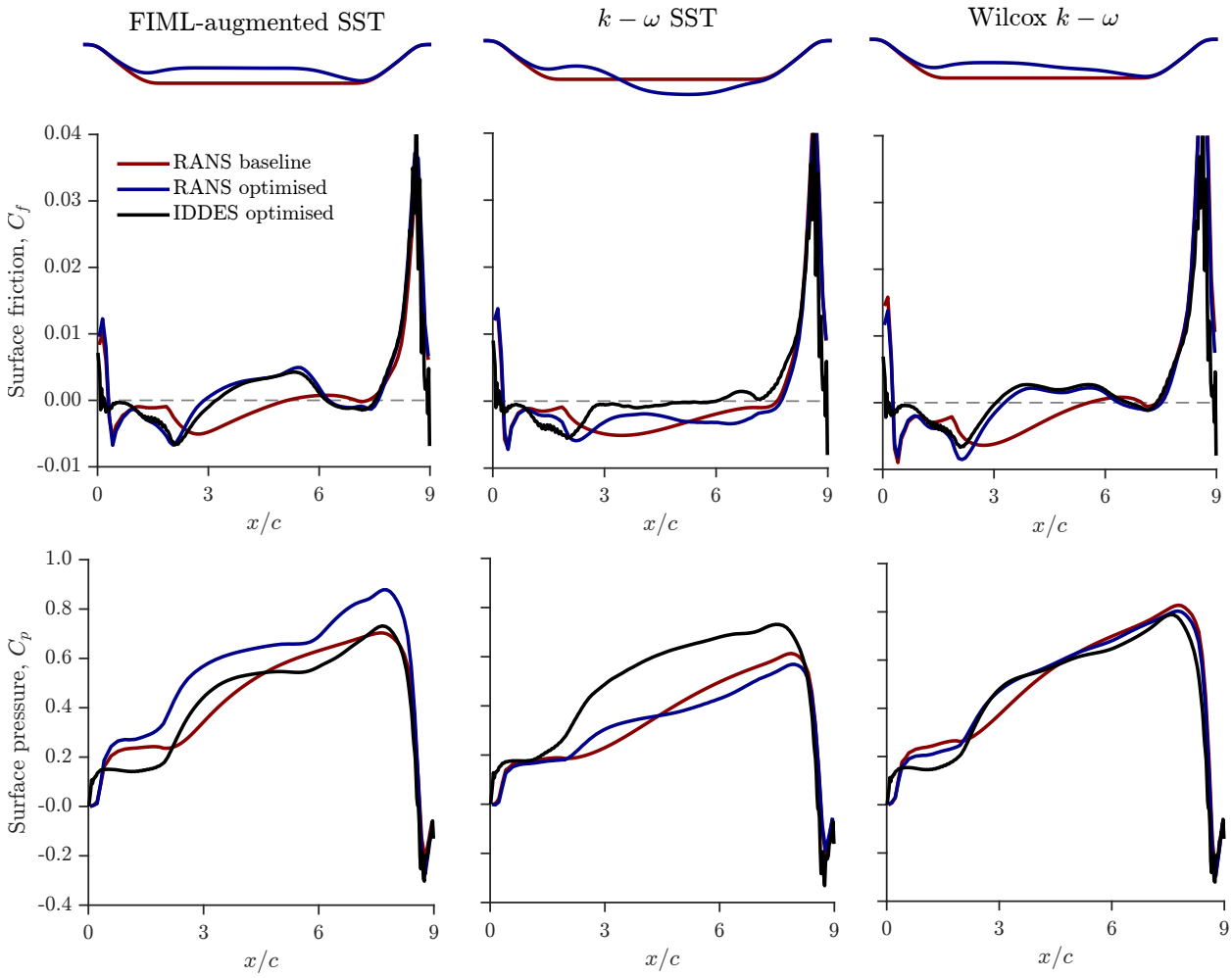

Fig. 9 The baseline shape overlaid with the optimised shapes for the three RANS-based turbulence models. The lower wall surface friction and surface pressure for the baseline and optimised shapes are also shown using the three respective turbulence models. In addition, IDDES predictions for the optimised shapes are shown for comparison.

2) Table 5 shows that the baseline $k-\omega$ SST model achieves the least drag reduction–based both on the RANS predictions and the IDDES results. The FIML-augmented $k-\omega$ SST and the Wilcox $k-\omega$ achieve considerably higher reductions. However, there are considerable errors between the RANS and IDDES predictions. This could be as a result of the issue in pressure predictions in the IDDES results, as discussed for the baseline shape in Sec III.A.
3) All three models attempt to reduce the drag in the baseline shape by decreasing the flow separation. The FIML augmented $k-\omega$ SST and the Wilcox $k-\omega$ achieve this by raising the lower wall. This results in a smaller separated shear layer compared to the baseline shape, as demonstrated by the earlier flow reattachment locations on the skin friction plots (Fig. 9), and the streamlines in Fig. 10. On the other hand, while the baseline $k-\omega$ SST reduces the size of the recirculation zone after the first hill, it introduces a second larger recirculation zone adjacent to the first one (based on the RANS predictions).
4) In all three cases reduction is achieved by decreasing the pressure drag (Table 6) while the viscous (or friction) components rise compared to the baseline shape (Table 4).
5) In terms of the skin friction predictions, the baseline $k-\omega$ SST model continues to be the most erroneous, similar to the baseline shape. Both the FIML-augmented $k-\omega$ SST and the Wilcox $k-\omega$ model predictions are similar to the IDDES.

6) For the surface pressure distributions, there are considerable discrepancies between the SST RANS models (both baseline and FIML-augmented), while the Wilcox $k-\omega$ predictions are similar. Again, further investigation is required to discern how accurate the IDDES predictions are before using these for benchmarking the RANS predictions.
7) The baseline $k-\omega$ SST model continues to over-predict the flow separation in the shear layer, in comparison to the IDDES results, as shown in the velocity contours in Fig. 7 and the streamwise velocity profiles in Fig. 11. The Wilcox $k-\omega$ model is somewhat more accurate in velocity predictions, however, discrepancies exist near the walls. On the other hand, the FIML-augmented $k-\omega$ SST match the IDDES velocity predictions fairly well (Fig. 11).
8) Finally, turbulent flow structures are visualised using the Q-criterion in Fig. 12. The baseline case has much larger structures near the hills. These are reduced by various degrees in the different optimised cases.

Table 5 Drag coefficient predictions for the optimised hill walls using the different models. C_d *RANS* column is the drag prediction by the turbulence model used during aerodynamic shape optimisation, i.e. the model in column one. ΔC_d is the percentage drag reduction compared to the baseline shape.

Optimisation case	C_d RANS	C_d IDDES	Error	ΔC_d RANS	ΔC_d IDDES
$k-\omega$ SST	0.035371	0.033291	6.25%	6.53%	4.52%
FIML-augmented SST	0.031191	0.026043	19.77%	20.81%	25.30%
Wilcox $k-\omega$	0.033695	0.027963	20.50%	35.30%	19.80%

Table 6 Predictions of drag components for the three turbulence model optimisation scenarios. $C_{d,p}$ and $C_{d,v}$ refer to the pressure and viscous (friction) forces.

Optimisation case	$C_{d,p}$ RANS	$C_{d,p}$ IDDES	$C_{d,v}$ RANS	$C_{d,v}$ IDDES
$k-\omega$ SST	0.03514	0.03211	0.00024	0.00119
FIML-augmented SST	0.02867	0.02423	0.00252	0.00181
Wilcox $k-\omega$	0.03132	0.02608	0.00237	0.00188

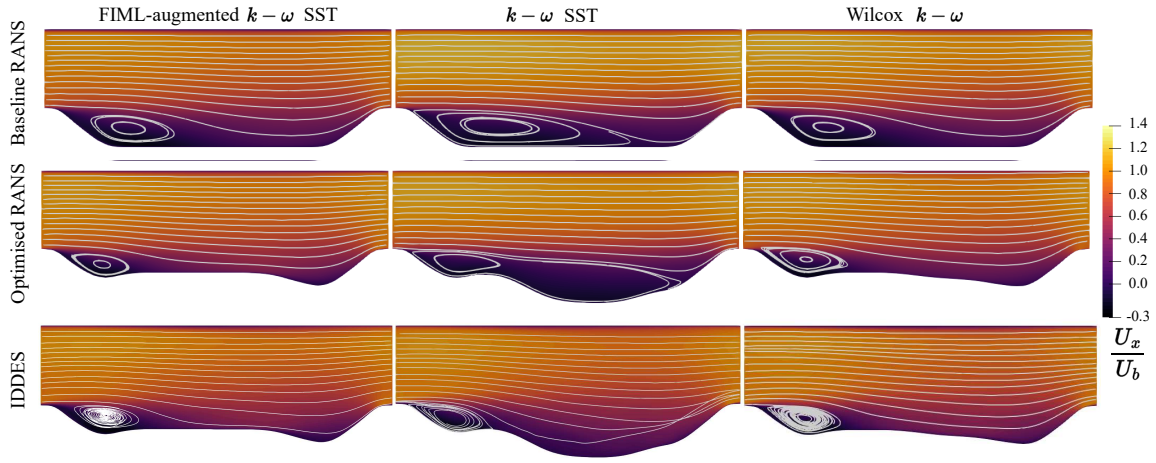

Fig. 10 The baseline and optimised streamlines with normalised streamwise velocity. The first two rows show the predictions from the respective RANS-based turbulence models used during the shape optimisation, while the final row shows the IDDES predictions of the optimised shapes.

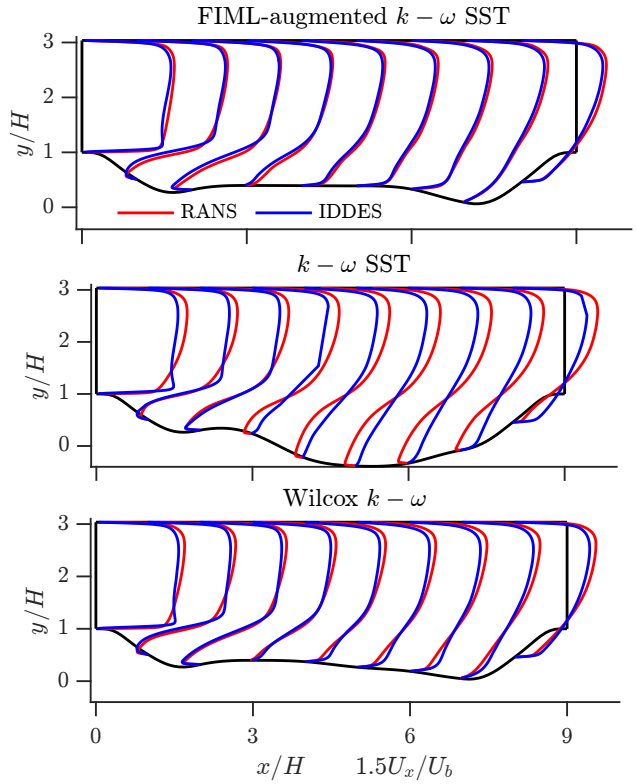

Fig. 11 Streamwise velocity profiles for the optimised shapes using the three different RANS models compared against the IDDES results.

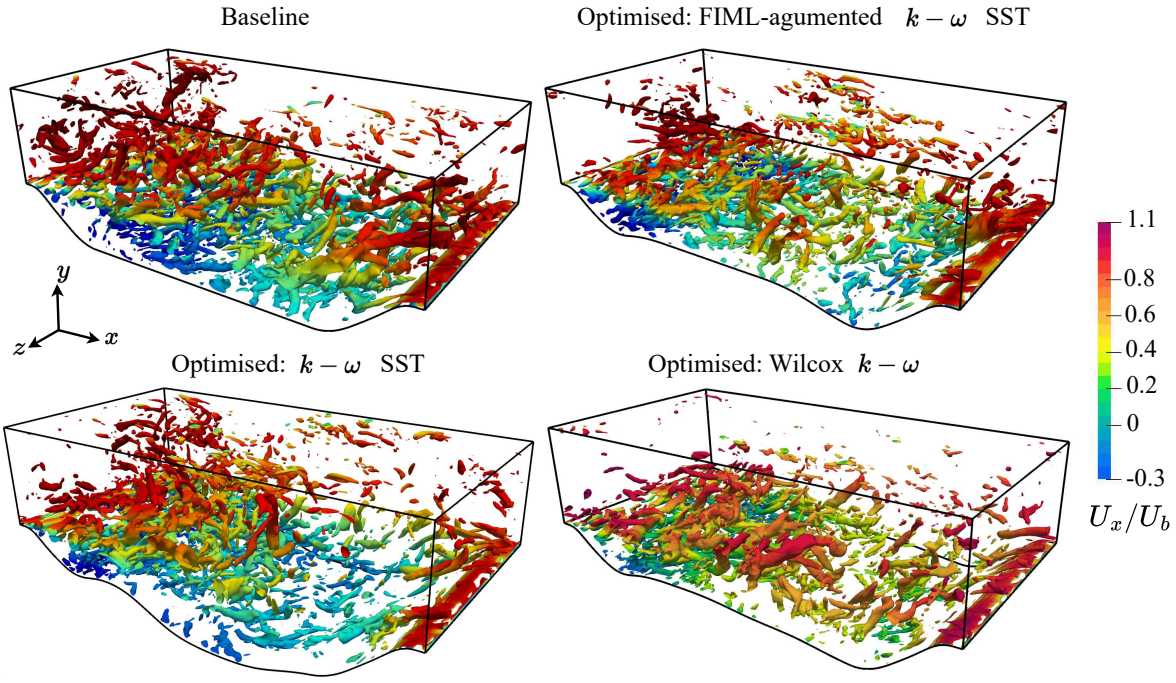

Fig. 12 Visualisation of the turbulent flow structures for the baseline and optimised shapes, using IDDES flow predictions. Contours show the Q-criterion, coloured by the normalised streamwise velocity.

IV. Conclusions

In this paper we presented an aerodynamic shape optimisation framework in which a RANS-based baseline turbulence model—$k-\omega$ shear stress transport (SST)—is augmented using the field inversion and machine learning (FIML) approach. The two-step process involved flow reconstruction through inverse modelling (an adjoint-based optimisation where the goal is to minimise the errors between some high-fidelity data and the baseline RANS model by applying a correction field, β, to the production term of the turbulent transport equation), and the generalisation of the β field using neural networks, used for predictions beyond the training dataset. The framework was applied to a proof of concept periodic hill case. Key steps and findings are summarised as follows:

1) We augmented the baseline $k-\omega$ SST model using the FIML approach. The augmented model was trained on DNS streamwise velocity fields for a set of parameterised periodic hills involving mild to massive flow separations. To test the effectiveness of the approach, we left the baseline geometry (starting point for shape optimisation) outside the training dataset.
2) The baseline SST model was shown to be very inaccurate in flow predictions of the baseline shape. It failed to accurately capture the separated flow in the shear layer, and over-estimated the size of the separation bubble.
3) The augmented $k-\omega$ SST model was able to significantly reduce the errors in most of the quantities of interest, and was shown to match reference DNS data well.
4) The adjoint-based aerodynamic shape optimisation was formulated as that of reducing the surface drag on the lower wall of the periodic hill geometry.
5) In order to demonstrate the inherent sensitivity of the shape optimisation outcome on the choice of RANS-based turbulence model for flow predictions, we also used the Wilcox $k-\omega$ model to perform shape optimisation. We also demonstrated that of the two existing (baseline) turbulence models considered, the Wilcox $k-\omega$ model was overall more accurate in terms of flow prediction comparisons to the reference DNS data.
6) We also proposed using a higher-fidelity approach to validate RANS-based flow predictions for the optimised shapes. For this, the Spalart-Allmaras based improved delayed detached eddy simulations (IDDES) was used. We validated the IDDES results against the available reference DNS data. While the IDDES results were much more accurate compared to the baseline RANS-based predictions in most quantities (velocity, Reynolds stress components, and skin friction), it failed to match the reference DNS pressure distribution. The cause of this discrepancy is subject to ongoing investigations.
7) The three different RANS-based turbulence models—baseline $k-\omega$ SST, FIML-augmented $k-\omega$ SST, and the Wilcox $k-\omega$—resulted in different optimal shapes, highlighting the sensitivity of the final outcome to the turbulence model.
8) The drag reductions were quantified both based on the respective RANS-based flow predictions of the baseline and optimised shapes, and the IDDES-based predictions, Table 5.
9) The baseline $k-\omega$ SST model led to the least drag reduction: $4.5-6.5\%$. The FIML-augmented $k-\omega$ SST model achieved a drag reduction of $20.8-25.3\%$. The Wilcox $k-\omega$ model achieved an error reduction of $19.8-35.3\%$.
10) In comparison to the IDDES predictions, the baseline $k-\omega$ SST model was the least accurate in terms of velocity and skin friction predictions. Both the Wilcox $k-\omega$ and the FIML-augmented $k-\omega$ SST model matched the skin friction and velocity predictions from IDDES fairly well.

Overall, the preliminary results demonstrate that creating augmented turbulence models using data-driven approaches (e.g. FIML) for aerodynamic shape optimisation in separated flows is a promising research topic, which requires further investigations. In the future we will also investigate: replacing the DNS training data with IDDES to ensure that the training data and validation data use a consistent approach (while still using the DNS data for IDDES validation), using different deep neural network architectures and features/inputs in the FIML training, increasing/reducing the number of parameterised shapes used for FIML training, and using different quantities for the training data, e.g. for the present results we only used the streamwise velocity fields, but could also use surface data such as skin friction and surface pressure.

Acknowledgement

Omid Bidar's work is funded by the University of Sheffield Engineering and Physical Sciences Research Council (EPSRC) Doctoral Training Partnership Scholarship.

References

[1] Slotnik, J., Khodadoust, A., Alonso, J., Darmofal, D., Gropp, W., Lurie, E., and Mavriplis, D., "CFD Vision 2030 Study: A Path to Revolutionary Computational Aerosciences," *Technical Report CR–2014-218178, NASA*, 2014. URL https://ntrs.nasa.gov/citations/20140003093.

[2] Martins, J. R., "Aerodynamic design optimization: Challenges and perspectives," *Computers & Fluids*, Vol. 239, 2022, p. 105391. https://doi.org/10.1016/j.compfluid.2022.105391.

[3] Su, W.-D., Zhao, H., Cai, Q.-D., Xiong, A.-K., and Wu, J.-Z., "A diagnosis of linear eddy-viscosity in turbulence modeling," *Physics of Fluids*, Vol. 14, No. 3, 2002, pp. 1284–1287. https://doi.org/10.1063/1.1436495.

[4] Li, J., Du, X., and Martins, J. R., "Machine learning in aerodynamic shape optimization," *Progress in Aerospace Sciences*, Vol. 134, 2022, p. 100849. https://doi.org/10.1016/j.paerosci.2022.100849.

[5] Vuruskan, A., and Hosder, S., "Impact of Turbulence Models and Shape Parameterization on Robust Aerodynamic Shape Optimization," *Journal of Aircraft*, Vol. 56, No. 3, 2019, pp. 1099–1115. https://doi.org/10.2514/1.c035039.

[6] Cook, L. W., Mishra, A. A., Jarrett, J. P., Willcox, K. E., and Iaccarino, G., "Optimization under turbulence model uncertainty for aerospace design," *Physics of Fluids*, Vol. 31, No. 10, 2019, p. 105111. https://doi.org/10.1063/1.5118785.

[7] Duraisamy, K., Iaccarino, G., and Xiao, H., "Turbulence Modeling in the Age of Data," *Annual Review of Fluid Mechanics*, Vol. 51, No. 1, 2019, pp. 357–377. https://doi.org/10.1146/annurev-fluid-010518-040547.

[8] Ling, J., Kurzawski, A., and Templeton, J., "Reynolds averaged turbulence modelling using deep neural networks with embedded invariance," *Journal of Fluid Mechanics*, Vol. 807, 2016, pp. 155–166. https://doi.org/10.1017/jfm.2016.615.

[9] Kaandorp, M. L., and Dwight, R. P., "Data-driven modelling of the Reynolds stress tensor using random forests with invariance," *Computers & Fluids*, Vol. 202, 2020, p. 104497. https://doi.org/10.1016/j.compfluid.2020.104497.

[10] Weatheritt, J., and Sandberg, R., "The development of algebraic stress models using a novel evolutionary algorithm," *International Journal of Heat and Fluid Flow*, Vol. 68, 2017, pp. 298–318. https://doi.org/10.1016/j.ijheatfluidflow.2017.09.017.

[11] Schmelzer, M., Dwight, R. P., and Cinnella, P., "Discovery of Algebraic Reynolds-Stress Models Using Sparse Symbolic Regression," *Flow, Turbulence and Combustion*, Vol. 104, No. 2-3, 2019, pp. 579–603. https://doi.org/10.1007/s10494-019-00089-x.

[12] Beetham, S., and Capecelatro, J., "Formulating turbulence closures using sparse regression with embedded form invariance," *Physical Review Fluids*, Vol. 5, No. 8, 2020. https://doi.org/10.1103/physrevfluids.5.084611.

[13] Xiao, H., and Cinnella, P., "Quantification of model uncertainty in RANS simulations: A review," *Progress in Aerospace Sciences*, Vol. 108, 2019, pp. 1–31. https://doi.org/10.1016/j.paerosci.2018.10.001.

[14] Duraisamy, K., "Perspectives on machine learning-augmented Reynolds-averaged and large eddy simulation models of turbulence," *Physical Review Fluids*, Vol. 6, No. 5, 2021. https://doi.org/10.1103/physrevfluids.6.050504.

[15] Duraisamy, K., Zhang, Z. J., and Singh, A. P., "New Approaches in Turbulence and Transition Modeling Using Data-driven Techniques," *53rd AIAA Aerospace Sciences Meeting*, American Institute of Aeronautics and Astronautics, 2015. https://doi.org/10.2514/6.2015-1284.

[16] Parish, E. J., and Duraisamy, K., "A paradigm for data-driven predictive modeling using field inversion and machine learning," *Journal of Computational Physics*, Vol. 305, 2016, pp. 758–774. https://doi.org/10.1016/j.jcp.2015.11.012.

[17] Singh, A. P., Medida, S., and Duraisamy, K., "Machine-Learning-Augmented Predictive Modeling of Turbulent Separated Flows over Airfoils," *AIAA Journal*, Vol. 55, No. 7, 2017, pp. 2215–2227. https://doi.org/10.2514/1.j055595.

[18] Holland, J. R., Baeder, J. D., and Duraisamy, K., "Field Inversion and Machine Learning With Embedded Neural Networks: Physics-Consistent Neural Network Training," *AIAA Aviation 2019 Forum*, American Institute of Aeronautics and Astronautics, 2019. https://doi.org/10.2514/6.2019-3200.

[19] Singh, A. P., and Duraisamy, K., "Using field inversion to quantify functional errors in turbulence closures," *Physics of Fluids*, Vol. 28, No. 4, 2016, p. 045110. https://doi.org/10.1063/1.4947045.

[20] He, C., Liu, Y., and Gan, L., "A data assimilation model for turbulent flows using continuous adjoint formulation," *Physics of Fluids*, Vol. 30, No. 10, 2018, p. 105108. https://doi.org/10.1063/1.5048727.

[21] Belligoli, Z., Dwight, R. P., and Eitelberg, G., "Reconstruction of Turbulent Flows at High Reynolds Numbers Using Data Assimilation Techniques," *AIAA Journal*, Vol. 59, No. 3, 2021, pp. 855–867. https://doi.org/10.2514/1.j059474.

[22] Bidar, O., He, P., Anderson, S., and Qin, N., "Turbulent Mean Flow Reconstruction Based on Sparse Multi-sensor Data and Adjoint-based Field Inversion," *AIAA AVIATION 2022 Forum*, American Institute of Aeronautics and Astronautics, 2022. https://doi.org/10.2514/6.2022-3900.

[23] Zhang, X.-L., Michelén-Ströfer, C., and Xiao, H., "Regularized ensemble Kalman methods for inverse problems," *Journal of Computational Physics*, Vol. 416, 2020, p. 109517. https://doi.org/10.1016/j.jcp.2020.109517.

[24] Zhang, X.-L., Xiao, H., He, G.-W., and Wang, S.-Z., "Assimilation of disparate data for enhanced reconstruction of turbulent mean flows," *Computers & Fluids*, Vol. 224, 2021, p. 104962. https://doi.org/10.1016/j.compfluid.2021.104962.

[25] Zhang, X.-L., Xiao, H., and He, G., "Assessment of Regularized Ensemble Kalman Method for Inversion of Turbulence Quantity Fields," *AIAA Journal*, 2021, pp. 1–11. https://doi.org/10.2514/1.j060976.

[26] Fidkowski, K. J., "Gradient-based shape optimization for unsteady turbulent simulations using field inversion and machine learning," *Aerospace Science and Technology*, Vol. 129, 2022, p. 107843. https://doi.org/10.1016/j.ast.2022.107843.

[27] Fröhlich, J., and von Terzi, D., "Hybrid LES/RANS methods for the simulation of turbulent flows," *Progress in Aerospace Sciences*, Vol. 44, No. 5, 2008, pp. 349–377. https://doi.org/10.1016/j.paerosci.2008.05.001.

[28] Xiao, H., Wu, J.-L., Laizet, S., and Duan, L., "Flows over periodic hills of parameterized geometries: A dataset for data-driven turbulence modeling from direct simulations," *Computers & Fluids*, Vol. 200, 2020, p. 104431. https://doi.org/10.1016/j.compfluid.2020.104431.

[29] Rapp, C., and Manhart, M., "Flow over periodic hills: an experimental study," *Experiments in Fluids*, Vol. 51, No. 1, 2011, pp. 247–269. https://doi.org/10.1007/s00348-011-1045-y.

[30] Balakumar, P., and Park, G. I., "DNS/LES Simulations of Separated Flows at High Reynolds Numbers," *45th AIAA Fluid Dynamics Conference*, American Institute of Aeronautics and Astronautics, 2015. https://doi.org/10.2514/6.2015-2783.

[31] Gloerfelt, X., and Cinnella, P., "Large Eddy Simulation Requirements for the Flow over Periodic Hills," *Flow, Turbulence and Combustion*, Vol. 103, No. 1, 2019, pp. 55–91. https://doi.org/10.1007/s10494-018-0005-5.

[32] Menter, F. R., "Two-equation eddy-viscosity turbulence models for engineering applications," *AIAA Journal*, Vol. 32, No. 8, 1994, pp. 1598–1605. https://doi.org/10.2514/3.12149.

[33] Menter, F. R., Kuntz, M., and Langtry, R., "Ten years of industrial experience with the SST turbulence model," *Turbulence, heat and mass transfer*, Vol. 4, No. 1, 2003, pp. 625–632.

[34] Bidar, O., He, P., Anderson, S., and Qin, N., "An Open-Source Adjoint-based Field Inversion Tool for Data-driven RANS modelling," *AIAA AVIATION 2022 Forum*, American Institute of Aeronautics and Astronautics, 2022. https://doi.org/10.2514/6.2022-4125.

[35] Ling, J., and Templeton, J., "Evaluation of machine learning algorithms for prediction of regions of high Reynolds averaged Navier Stokes uncertainty," *Physics of Fluids*, Vol. 27, No. 8, 2015, p. 085103. https://doi.org/10.1063/1.4927765.

[36] Wang, J.-X., Wu, J.-L., and Xiao, H., "Physics-informed machine learning approach for reconstructing Reynolds stress modeling discrepancies based on DNS data," *Physical Review Fluids*, Vol. 2, No. 3, 2017. https://doi.org/10.1103/physrevfluids.2.034603.

[37] Volpiani, P. S., Meyer, M., Franceschini, L., Dandois, J., Renac, F., Martin, E., Marquet, O., and Sipp, D., "Machine learning-augmented turbulence modeling for RANS simulations of massively separated flows," *Physical Review Fluids*, Vol. 6, No. 6, 2021. https://doi.org/10.1103/physrevfluids.6.064607.

[38] Maulik, R., Sharma, H., Patel, S., Lusch, B., and Jennings, E., "Deploying deep learning in OpenFOAM with TensorFlow," *AIAA Scitech 2021 Forum*, American Institute of Aeronautics and Astronautics, 2021. https://doi.org/10.2514/6.2021-1485.

[39] He, P., Mader, C. A., Martins, J. R. R. A., and Maki, K. J., "DAFoam: An Open-Source Adjoint Framework for Multidisciplinary Design Optimization with OpenFOAM," *AIAA Journal*, Vol. 58, No. 3, 2020, pp. 1304–1319. https://doi.org/10.2514/1.j058853.

[40] Chaouat, B., "The State of the Art of Hybrid RANS/LES Modeling for the Simulation of Turbulent Flows," *Flow, Turbulence and Combustion*, Vol. 99, No. 2, 2017, pp. 279–327. https://doi.org/10.1007/s10494-017-9828-8.

[41] Shur, M. L., Spalart, P. R., Strelets, M. K., and Travin, A. K., "A hybrid RANS-LES approach with delayed-DES and wall-modelled LES capabilities," *International Journal of Heat and Fluid Flow*, Vol. 29, No. 6, 2008, pp. 1638–1649. https://doi.org/10.1016/j.ijheatfluidflow.2008.07.001.

[42] Krank, B., Kronbichler, M., and Wall, W. A., "Direct Numerical Simulation of Flow over Periodic Hills up to $Re_H = 10,595$," *Flow, Turbulence and Combustion*, Vol. 101, No. 2, 2018, pp. 521–551. https://doi.org/10.1007/s10494-018-9941-3.